Riding safety prediction of a high-speed train running on transition zone under foundation settlement

Peng, Borong; He, Xuhui; Xu, Lei; Li, Zheng; Guo, Yunlong

DOI
10.1016/j.advengsoft.2024.103757

Publication date
2024

Document Version
Final published version

Published in
Advances in Engineering Software

Advances in Engineering Software 197 (2024) 103757

Contents lists available at ScienceDirect

Advances in Engineering Software

journal homepage: www.elsevier.com/locate/advengsoft

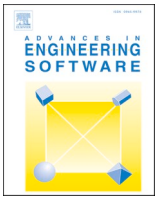

Research paper

Riding safety prediction of a high-speed train running on transition zone under foundation settlement

Borong Peng [a], Xuhui He [a,b], Lei Xu [a,b], Zheng Li [a], Yunlong Guo [c,d,*]

[a] School of Civil Engineering, Central South University, Changsha, Hunan, China
[b] National Engineering Laboratory for High-Speed Railway Construction, Changsha 410075, China
[c] Faculty of Civil Engineering and Geosciences, Delft University of Technology, Delft 2628CN, 7 Netherlands
[d] Department of Civil Engineering, School of Engineering, University of Birmingham, Birmingham B152TT, United Kingdom

ARTICLE INFO

Keywords:
Pier settlement
Transition zone
High-speed railway
Vehicle riding safety
Rail deformation
Time-frequency analysis

ABSTRACT

The settlement of piers and subgrade bending deformation are widely recognized as common issues in the transition zones of high-speed railway bridges. This study aims to investigate the settlement behavior within these transition zones and its impact on the dynamic interaction between trains and the track. To achieve this, a vehicle-track-transition zone mapping relationship model is developed to analyze both the settlement behavior and the resulting dynamic response characteristics. The study employs the finite element method and multi-body dynamics to construct the simulation model. Settlement effects are simulated using the Newton-Raphson iterative method, with the additional rail deformation caused by foundation settlement serving as the excitation for the vehicle-track-transition zone dynamic interaction system. In the numerical analysis, the dynamic effects of three key factors—train speed, transition zone length, and the amplitude of foundation settlement—are examined based on the performance of the vehicle-track-transition zone interaction. The time-frequency technique is utilized to comprehensively reveal and clarify the spatial-frequency characteristics of system responses influenced by settlement excitation. Moreover, the relationship between the safety-based settlement threshold and these three factors is calibrated.

1. Introduction

1.1. Research background

With the rapid development of high-speed railways (HSR), the evaluation of high-speed train's riding safety becomes a significant task for related engineers and scholars [1-3]. It has been reported frequently that the settlement of railway substructures is a severe factor that affects the dynamic performance of the train-structure interaction system and deteriorates the service safety of HSR [4-8]. As a specific type of railway substructure, the bridge-subgrade transition zone suffers from a larger settlement than that of the common bridge/subgrade zones owing to the varying stiffness in the longitudinal direction. The settlement of the transition zone brings uncertainty to the assessment work about train-induced vibration and train riding safety. Therefore, it is necessary to predict the dynamic effects of the settlement at the transition zone on the train-structure interaction system.

In the last decades, studies have been made to the prediction of track deformation subjected to the railway substructure settlement and the dynamic evaluation of the train-induced vibrations under the settlement has been further conducted. As for the subgrade settlement, for instance, Wang et al. [9-11] established a validated numerical model to predict the permanent settlement of track under the cumulative deformation of the subgrade, in which the dynamic behavior of the moving train was fully discussed. Furthermore, Shan et al. [12-13] proposed an effective dynamic interaction model to estimate the cumulative settlement of the soil of transition zones caused by the cyclic train loads, and the dynamic stress-strain of the soil in the different periods is fully revealed. Notably, in the works of Varandas et al. [14-15], the time history of ballast pressure shows an obvious temporal and spatial variation phenomenon, especially for the unsupported sleepers that occur in the settlement area. The detailed dynamic evaluation work has been conducted by Paixao et al. [16]. In their study, the effects of the settlement of subgrade soil and the induced hanging sleepers on the dynamic behavior of the train-track-soil interaction system were analyzed. Analogously, Nasrollahi et al. [17] presented a simple iterative method to predict long-term

* Corresponding author.
E-mail address: yunlong.guo@tudelft.nl (Y. Guo).

https://doi.org/10.1016/j.advengsoft.2024.103757
Received 8 May 2024; Received in revised form 21 July 2024; Accepted 11 August 2024
Available online 16 August 2024

differential settlement in the transition zone by considering the time-varying characteristics of the finite element model, where the dynamic responses, settlement, and contact pressures are updated in each iterative step. Sun et al. [18] introduced track–subgrade dynamic stresses induced by a high-speed vehicle into the empirical power mode to study the dynamic behavior under the subgrade settlement.

As for the pier settlement, the related works were performed to realize the "mapping relationship" between the track deformation and bridge deformation under the settlement. Chen et al. [19-20] deduced the functional relationship between rail deformation and bridge deformation, and the effectiveness and practicality of the model were validated by comparing it with the finite element model established in the software ANSYS. To describe the influence of pier settlement on the non-linear contact behavior between baseplate and bridge accurately, the generation mechanism of that is discussed in this work [21]. In his further study [22], the various important factors including self-weight creep shrinkage rail random irregularity and temperature are incorporated into analysis of the riding safety under pier settlement and then the pier settlement limit value can be determined. Gou et al. [23-24] improved the mapping relationship function by introducing the differential equation of continuous and noncontinuous Euler beams, where the interlayered contact behavior of track and bridge are fully considered. The dynamic evaluation of the train-bridge system was conducted by Yau et al. [25], in which the force-element balance method is adopted to predict the bridge deformation that is regarded as the geometric excitation of the train-bridge system. In further research, how to control the settlement has aroused extensive attention. Richard et al. [26] proposed a new method using competent caliche layers bonded to the top and bottom of a continuous flight auger pile as a new composite foundation system named caliche stiffened pile, which can efficiently control the pier settlement. To further elucidate the importance of this study, the pier settlement within the Beijing-Tianjin intercity railway mileage JJK15+000-JJK15+900 is monitored, and the change value of pier settlement from December 2009 to September 2012 is shown in Fig. 1. It is not difficult to find that the maximum pier settlement reaches 54.6mm, so a versatile model for predicting the riding safety is significant for engineerers.

To achieve a more accurate assessment of the train-induced vibrations under the substructure settlement, a precise dynamic interaction model should be established. Zhai et al. and Xia et al. [27-30] made strides in the improvement of the simulation model for the train-structure interaction. In their contributions, the wheel-rail contact geometries in both normal and tangent directions of the contact points are described. The breakthrough of the wheel-rail rigid contact hypothesis into the spatial elastic contact brings comprehensive insight into the wheel motions under the random track irregularities. In order to solve the problem that the time step of the force-element balance method is difficult to converge, Xu et al. [31] proposed a matrix coupling method for the three-dimensional rail system. Li et al. [32] verified the accuracy of the 2D model by comparing the dynamic responses of 2D and 3D models treated by the infinite element boundary.

Regarding the state-of-the-art research, it can be found that the current research mainly focuses on the dynamic response of train-structure interaction under the substructure settlement. However, there is little research about the riding safety of the high-speed train undergoing the settlement.

1.2. The scope of the research

This paper focuses on the riding safety of the bridge-subgrade transition zone under the settlement. An effective dynamic model is established, and the influence of the two typical types of settlements at the transition zones (namely the pier settlement and subgrade bending settlement) on the dynamic performance of the vehicle-track-transition zone interaction system is discussed. The settlements are treated as the additional geometric excitation to the wheel-rail interaction system. The various vehicle running speeds and transition zone lengths are discussed to estimate the safety-based settlement thresholds.

The following paper is organized as follows:

(1) In Section 2, the basic the vehicle-track-transition zone interaction is established, and some methods with viscoelastic boundary are introduced.
(2) In Section 3, the rail deformation induced by foundation settlement is considered as additional rail irregularity, which is introduced into the dynamic interaction model.
(3) In Section 4, based on the riding safety of high-speed trains, the threshold of the foundation settlement is calculated.
(4) In Section 5, conclusions are drawn from the numerical studies.

2. Vehicle track-transition zone dynamic interaction model

Fig. 2 shows the theoretical model of the vehicle-track-transition zone dynamic interaction. The bridge system consists of 5-span simply supported beams with a span of 32 m. The soil at the transition zone deals with stiffness-varying characteristics in the longitudinal direction. The vehicle system is modeled as a multi-rigid body with primary and secondary suspension systems. The three sub-systems are coupled by the interaction force and the model boundary is constrained by bearing stiffness and viscoelastic boundary to eliminate the influence of wave

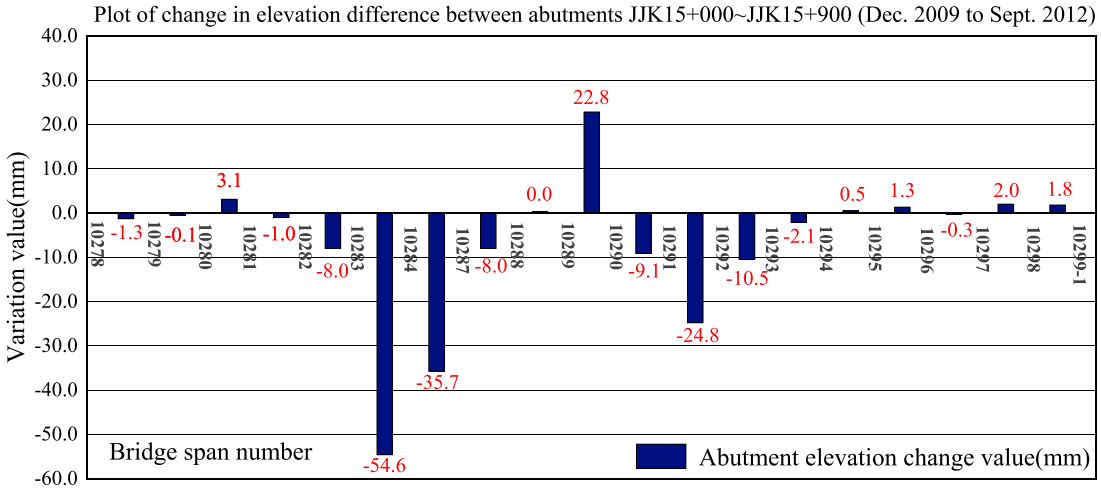

Fig. 1. Pier settlement monitoring diagram.

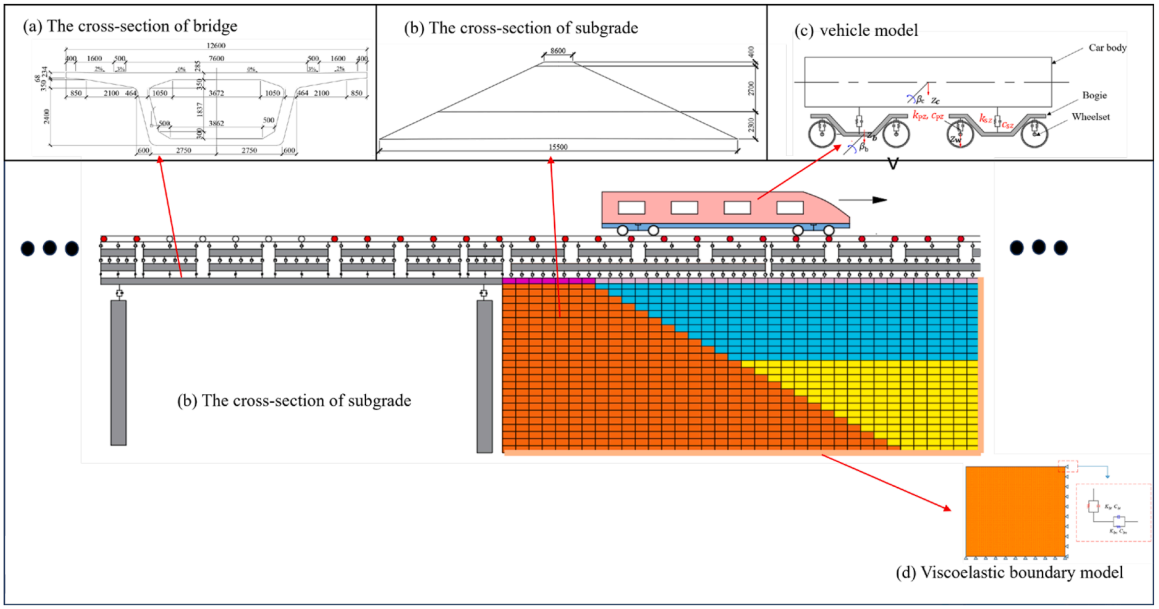

Fig. 2. Schematic diagram of the proposed theoretical model (m).

reflection as much as possible.

This paper employs a matrix coupled model that satisfies the principle of displacement coordination and force element equilibrium, ensuring numerical analysis stability. Various numerical integration methods are applicable for dynamically calculating this system, so the *Newmark-β method* is applied to solve this dynamic system.

The vehicle track-transition zone dynamic model follows the assumption:

(1) Foundation settlement primarily affects the vertical deformation of the rail, so the dynamic system is simplified to a 2D dynamic model.
(2) The track structures remain intact with no indications of damage.
(3) The substructure component is simulated as a layered isotropic linear elastic material.
(4) The bending deformation in transition zone is assumed straight line.

2.1. Fundamental approach for modeling the sub-models

2.1.1. Track sub-model

The mass matrix of the track system is derived from the negative work done by the inertial forces of the rail, slab, and baseplate, and can be expressed as:

$$\mathbf{M}_{\mathrm{TT}} = \sum_{n_r}\sum_{l_r}\mathbf{M}_r^e + \sum_{n_{s1}}\sum_{n_{s2}}\mathbf{M}_s^e + \sum_{n_{p1}}\sum_{n_{p2}}\mathbf{M}_p^e \tag{1}$$

with $\mathbf{M}_r^e = \frac{m_r}{2}\int_0^{l_r}\mathbf{N}_r^T\mathbf{N}_r dx$, $\mathbf{M}_s^e = \frac{m_s h_s w_s}{2}\int_0^{l_s}\mathbf{N}_s^T\mathbf{N}_s dx$, $\mathbf{M}_p^e = \frac{m_p h_p w_p}{2}\int_0^{l_p}\mathbf{N}_p^T\mathbf{N}_p dx$, where $\mathbf{M}_r^e$, $\mathbf{M}_s^e$, and $\mathbf{M}_p^e$represents the mass matrix of the rail, slab, and baseplate; $m_r$denote mass per length of the rail; $m_s$and m_p denote the density of the slab and baseplate, respectively; h_s and h_p represent the height of the slab and baseplate; w_s and $w_p$represent the width of the slab and baseplate; l_r, l_s and l_r represent the longitudinal length of the rail, slab, and baseplate element; N_r, N_s, and N_p represent the shape function matrix; n_{s1} and n_{p1} represent the number of slab and baseplate, respectively; n_{s2} and n_{p2} represent the number of elements per slab and baseplate, respectively.

$$\mathbf{K}_{TT} = \sum_{n_r}\sum_{l_r}\mathbf{K}_r^e + \sum_{n_{s1}}\sum_{n_{s2}}\mathbf{K}_s^e + \sum_{n_{p1}}\sum_{n_{p2}}\mathbf{K}_p^e \tag{2}$$

with $\mathbf{K}_r^e = \frac{E_r I_r}{2}\int_0^{l_r}\left(\frac{\partial^2[\mathbf{N}_r]}{\partial x^2}\right)^T\left(\frac{\partial^2[\mathbf{N}_r]}{\partial x^2}\right)dx$; $\mathbf{K}_s^e = \frac{E_s I_s}{2}\int_0^{l_s}\left(\frac{\partial^2[\mathbf{N}_s]}{\partial x^2}\right)^T\left(\frac{\partial^2[\mathbf{N}_s]}{\partial x^2}\right)dx$;

$\mathbf{K}_p^e = \frac{E_p I_p}{2}\int_0^{l_p}\left(\frac{\partial^2[\mathbf{N}_p]}{\partial x^2}\right)^T\left(\frac{\partial^2[\mathbf{N}_p]}{\partial x^2}\right)dx.$

Where E_r, E_s and E_p represent the elastic modulus of the rail, slab, and baseplate; I_r, I_s and I_p represent the moment of inertia of the track slab and baseplate. the parameters are shown in **appendix. I**.

2.1.2. Bridge sub-model

The bridge with a span of 32 m is modeled by beam elements. Its cross-section is shown in Fig. 2**(a)** and stiffness matrices are generated by

$$\begin{cases}\mathbf{M}_b = \sum_{n_{b1}}\sum_{n_{b2}}\mathbf{M}_b^e \\ \mathbf{K}_b = \sum_{n_{b1}}\sum_{n_{b2}}\mathbf{K}_b^e + \mathbf{K}_{br,i} \\ \mathbf{C}_b = \alpha\mathbf{M}_b + \beta\mathbf{K}_b\end{cases} \tag{3}$$

with $\mathbf{M}_b^e = \frac{m_b h_b w_b}{2}\int_0^{l_b}\mathbf{N}_b{}^T\mathbf{N}_b\mathrm{d}x$; $\mathbf{K}_b^e = \frac{E_b I_b}{2}\int_0^{l_b}\left(\frac{\partial^2[\mathbf{N}_b]}{\partial x^2}\right)^T\left(\frac{\partial^2[\mathbf{N}_b]}{\partial x^2}\right)dx$. where $\mathbf{M}_b^e$ and $\mathbf{K}_b^e$ represent the element mass and stiffness matrix of the bridge; $\mathbf{K}_{br,i}$representing the stiffness of the 'i-th' bearing. αand β are mass proportion and stiffness proportion; $\mathbf{N}_b$is the bridge shape function. E_b is the elastic model of the bridge; I_b is the moment of inertia of the bridge.

The natural vibration frequencies of the bridge are obtained by the subspace iteration method. The Rayleigh damping method is adopted to depict the visco-elastic damping of the bridge.

2.1.3. Subgrade sub-model

As the quadrilateral element performs well in the simulation of the mechanical properties of soil, as shown in Fig. 2**(b)**. it is adopted to simulate the subgrade part of the model. The stiffness matrix and mass matrix are obtained by Eq. (4). The inverted trapezoidal subgrade is

adopted in the transition section, and the soil parameters used in the transition section are shown in **Appendix II.**

$$\begin{cases} \mathbf{M}_s = \sum_{n_{s,1}} \sum_{n_{s,2}} \mathbf{M}_s^e \\ \mathbf{K}_s = \sum_{n_{s,1}} \sum_{n_{s,2}} \mathbf{K}_s^e \end{cases} \tag{4}$$

with $\mathbf{M}_s^e = l_w \int\int [\mathbf{N}_s]^T [\rho_s][\mathbf{N}_s] dxdy$; $\mathrm{K}_s^e = l_w \int\int [\mathbf{B}_s]^T [\mathbf{D}_s][\mathbf{B}_s] dxdy$;

$$\begin{cases} [\mathbf{B}_{s,i}] = \begin{bmatrix} \frac{\partial N_{s,i}}{\partial x} & 0 \\ 0 & \frac{\partial N_{s,i}}{\partial y} \\ \frac{\partial N_{s,i}}{\partial y} & \frac{\partial N_{s,i}}{\partial x} \end{bmatrix} \\ [\mathbf{B}_s] = [\mathbf{B}_{s,1}, \mathbf{B}_{s,2}, \mathbf{B}_{s,3}, \mathbf{B}_{s,4}] \end{cases}$$

$$\mathrm{D}_s = diag\left(\frac{E_s}{(1+\mu_s)(1-2\mu_s)} \begin{bmatrix} 1 & \frac{\mu_s}{1-\mu_s} & 0 \\ \frac{\mu_s}{1-\mu_s} & 1 & 0 \\ 0 & 0 & \frac{1-2\mu_s}{2(1-\mu_s)} \end{bmatrix} \right).$$

where M_s^e and $\mathbf{K}_s^e$ represents the element mass and stiffness of the soil, $n_{s,1}$ denote the number of single-layer soil elements along the riding direction and the number of vertical single-layer soil elements; N_s denotes the function of the soil element, while the 'i' denotes the of the i-th node in the element; D_s is the elastic matrix for describing the constitutive relationship of the subgrade soil; E_s, μ_s and $\rho_s$are the elastic modulus, Poisson, ratio, and density respectively. J is the Jacobian matrix for constructing the geometric mapping relationship, dxdy = |J| dξdη.

The viscoelastic boundary [33] is utilized here to reduce the boundary reflection, as schematically shown in Fig. 2**(d)**. The viscoelastic boundary that includes the dampers and springs can be calculated by

$$\begin{cases} K_{\mathrm{bt}} = \alpha_{\mathrm{t}} \frac{G}{R}, K_{\mathrm{bn}} = \alpha_{\mathrm{n}} \frac{G}{R} \\ C_{\mathrm{bt}} = \rho C_{\mathrm{s}}, C_{\mathrm{bn}} = \rho C_{\mathrm{p}} \end{cases} \tag{5}$$

ere K_{bt} and K_{bn} denote the tangential and normal stiffness of the spring element, $C_{bt}$and C_{bn}denote the tangential and damping stiffness of the spring element; $C_p$and C_{s} are the symbol of the P wave and S wave propagating in the soil; ρ is the medium mass.

2.1.4. Vehicle sub-model

The vehicle model is modeled as a multibody consisting of one car body, two bogies, and four wheelsets. There are 2 degrees of freedom (DOFs) (vertical- and pitch-motion) for the car body and the bogie frame, and 1 DOF (vertical-motion) for each wheelset. The 2D vertical model is shown in Fig. 2**(c)**.

Based on the energy principle, the stiffness, damping, and mass matrices of vehicle system can be written as

$$\begin{cases} \mathbf{K}_{\mathrm{VV}} = \mathbf{K}_{\mathrm{p,z}} + \mathbf{K}_{\mathrm{s,z}} \\ \mathbf{C}_{\mathrm{VV}} = \mathbf{C}_{\mathrm{p,z}} + \mathbf{C}_{\mathrm{s,z}} \\ \mathbf{M}_{\mathrm{VV}} = \mathrm{diag}\left(\mathbf{M}_{\mathrm{c}}, \mathbf{M}_{\mathrm{fb}}, \mathbf{M}_{\mathrm{rb}}, \mathbf{M}_{\mathrm{w1}}, \mathbf{M}_{\mathrm{w2}}, \mathbf{M}_{\mathrm{w3}}, \mathbf{M}_{\mathrm{w4}}\right) \end{cases} \tag{6}$$

where the subscripts 'c', 'b', and 'w' represent the car body, the bogie, and the wheels; 'f' and 'r' denote the primary suspension system and secondary suspension system, respectively, and 'p' and 's' denote the primary and secondary suspension systems; the subscript 'V' represents the vehicle; the subscript 'z' is the symbol of vertical direction.

2.2. Coupling of the sub-systems

2.2.1. Multi-scale coupling approach

The substructure matrix is coupled to form the final matrix. We use spring and damping elements to simulate the interaction of substructure. In order to increase the calculation accuracy, the multi-scale coupling method is adopted between the track plate and the baseplate, and between the base plate and the subgrade, in Ref. [34]. The following takes the coupling of subgrade and baseplate as an example to analyze the multi-scale coupling method. The subgrade and baseplate have different local coordinates during integral operations due to their different divisions, as shown in Fig. 3. Therefore, when we calculate the subgrade-baseplate interaction matrix, each element needs to use different coordination transformations to meet the consistency and coordination of stiffness and damping, calculated by

$$\begin{cases} \mathbf{K}_{ss} = k_{ss} \int\int [\mathbf{N}_{BS}(x)]^{\mathrm{T}} \mathbf{N}_{BS}(x) dx \\ \mathbf{C}_{ss} = c_{ss} \int\int [\mathbf{N}_{BS}(x)]^{\mathrm{T}} \mathbf{N}_{BS}(x) dx \end{cases} \tag{7}$$

with $\mathbf{N}_{BS} = \mathbf{N}_B - \mathbf{N}_S$, $\widetilde{x} = x + x_0$where $\mathbf{N}$ denotes the shape function. B and S denote the baseplate and subgrade, respectively; k_{ss} and c_{ss} denote stiffness and damping of interaction parameters. $\widetilde{x}$ represents the node coordinates of subgrade elements after coordinate transformation.

2.2.2. Coupling matrix for wheel-rail contact relationship

The wheel-rail contact is simulated by introducing the Hertz contact theory, where the transient contact stiffness of wheel-rail impacts is calculated by

$$K_r = \frac{\left(\frac{1}{G}\Delta z\right)^{3/2}}{\Delta z} \widetilde{x} \tag{8}$$

where G is the Hertzian contact constant; Δz denotes the relative displacement between the wheel and rail.

Based on Xu's work [35], the wheel-rail contact model can be generated by introducing the "virtual degree of freedom" method, as shown in Fig. 4.

The relative displacement between wheel and rail is calculated by

$$d_r = D_{R1} + D_I \tag{9}$$

$$\Delta_r = D_W - D_{R1} - D_I \tag{10}$$

where D_{R} and D_{W} represent the dynamic displacement of the interacting rail and wheel respectively; D_{I} represents the rail irregularity; subscripts '$R1$', 'I' and 'W' denote the virtual rail, virtual irregularity, and wheel, respectively.

According to the relative displacement between wheel and rail, the corresponding Hertzian stiffness as shown in Eq. (8), and then the coupling matrix k_i is established as

$$\begin{cases} k_H = 0; \Delta r < 0 \\ k_H = \Pi(\Delta r); \Delta r \geq 0 \end{cases} \tag{11}$$

$$k_i = k_H \mathbf{N}^T \mathbf{N} \tag{12}$$

with $\mathbf{N} = [1, -1, -1]$, where Π is the Lagrange interpolation function; k_i denotes the virtual degree of freedom coupling matrix between wheel and rail. k_i is placed into the wheel-rail matrix according to the degree of freedom position, while $i = 1 \sim 4$ denotes the number of wheels.

As seen in Fig. 4, the length of the rail element is inconsistent with the vehicle running mileage $V \times \Delta t$; the time-varying contact points at the rail need to be updated, that is, the coupled matrix of wheel-rail

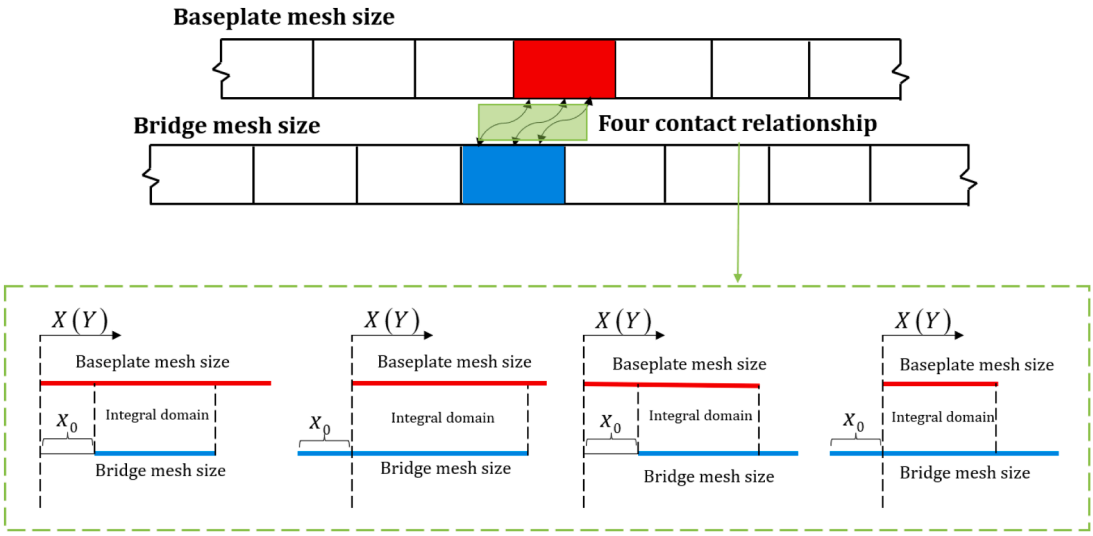

Fig. 3. Diagram of the integration domain of baseplate-subgrade interaction.

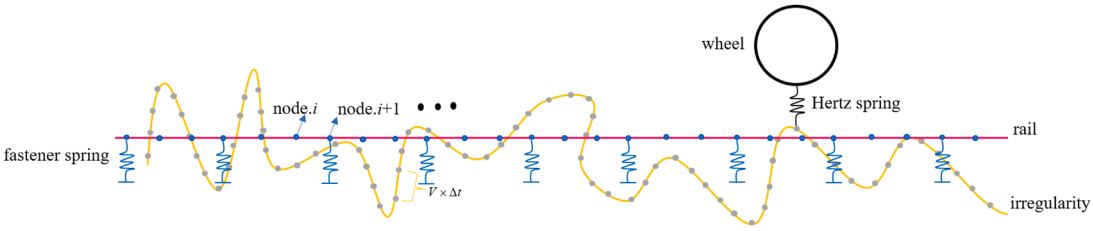

Fig. 4. Wheel-rail virtual contact method.

interaction should be redistribution in the global dynamic matrices. The principle is that the position of the train running to the virtual rail element is converted to the corresponding real rail element node according to the shape function, and the stiffness matrix $\mathbf{K}_{C1}$ is transformed into $\mathbf{K}_C$to realize the update of the real-time wheel-rail interaction system.

$$\mathbf{K}_C\left(\left[\Theta_{w,i},\Theta_{R,i},\Theta_{I,i}\right],\Theta_{R,i}\right)=\mathbf{K}_{C1}\left(\left[\Theta_{w,i},\Theta_{R1,i},\Theta_{I,i}\right],\Theta_{R1,i}\right)\mathbf{N}_{r,i} \tag{13}$$

$$\mathbf{K}_C\left(\Theta_{R,i},\left[\Theta_{w,i},\Theta_{R,i},\Theta_{I,i}\right]\right)=\mathbf{N}_{r,i}^T\mathbf{K}_{C1}\left(\Theta_{R1,i},\left[\Theta_{w,i},\Theta_{R1,i},\Theta_{I,i}\right]\right) \tag{14}$$

$$\mathbf{K}_C\left(\Theta_{wR,i},\Theta_{wR,i}\right)=\mathbf{K}_{C1}\left(\Theta_{R1,i},\Theta_{R1,i}\right)\mathbf{N}_{r,i} \tag{15}$$

where Θ the degree of freedom; R represents the real rail; N_r represents the element shape function of the rail beam under the corresponding wheel.

With the update of the wheel-rail coupled matrix, the dynamic equation can be written as

$$\begin{bmatrix}\mathbf{K}_{WW}&\mathbf{K}_{WR}&\mathbf{K}_{WI}\\\mathbf{K}_{RW}&\mathbf{K}_{RR}&\mathbf{K}_{RI}\\\mathbf{K}_{IW}&\mathbf{K}_{IR}&\mathbf{K}_{II}\end{bmatrix}\begin{bmatrix}\mathbf{D}_W\\\mathbf{D}_R\\\mathbf{D}_I\end{bmatrix}+\begin{bmatrix}\mathbf{C}_{WW}&\mathbf{C}_{WR}&\mathbf{C}_{WI}\\\mathbf{C}_{RW}&\mathbf{C}_{RR}&\mathbf{C}_{RI}\\\mathbf{C}_{IW}&\mathbf{C}_{IR}&\mathbf{C}_{II}\end{bmatrix}\begin{bmatrix}\dot{\mathbf{D}}_W\\\dot{\mathbf{D}}_R\\\dot{\mathbf{D}}_I\end{bmatrix}\cdots$$
$$+\begin{bmatrix}\mathbf{m}_{WW}&\mathbf{m}_{WR}&\mathbf{m}_{WI}\\\mathbf{m}_{RW}&\mathbf{m}_{RR}&\mathbf{m}_{RI}\\\mathbf{m}_{IW}&\mathbf{m}_{IR}&\mathbf{m}_{II}\end{bmatrix}\begin{bmatrix}\ddot{\mathbf{D}}_W\\\ddot{\mathbf{D}}_R\\\ddot{\mathbf{D}}_I\end{bmatrix}=\begin{bmatrix}\mathbf{P}_W\\\mathbf{P}_R\\\mathbf{P}_I\end{bmatrix} \tag{16}$$

Then the virtual degree of freedom under rail irregularity is processed and the coupling matrix of wheel-rail interaction can be obtained:

$$\begin{bmatrix}\mathbf{K}_{WW}&\mathbf{K}_{WR}\\\mathbf{K}_{RW}&\mathbf{K}_{RR}\end{bmatrix}\begin{bmatrix}\mathbf{D}_W\\\mathbf{D}_R\end{bmatrix}+\begin{bmatrix}\mathbf{C}_{WW}&\mathbf{C}_{WR}\\\mathbf{C}_{RW}&\mathbf{C}_{RR}\end{bmatrix}\begin{bmatrix}\dot{\mathbf{D}}_W\\\dot{\mathbf{D}}_R\end{bmatrix}+\begin{bmatrix}\mathbf{m}_{WW}&\mathbf{m}_{WR}\\\mathbf{m}_{RW}&\mathbf{m}_{RR}\end{bmatrix}\begin{bmatrix}\ddot{\mathbf{D}}_W\\\ddot{\mathbf{D}}_R\end{bmatrix}$$
$$=\begin{bmatrix}\mathbf{P}_W-\mathbf{K}_{WI}\mathbf{D}_I-\mathbf{C}_{WI}\dot{\mathbf{D}}_I-\mathbf{m}_{WI}\ddot{\mathbf{D}}_W\\\mathbf{P}_R-\mathbf{K}_{RI}\mathbf{D}_I-\mathbf{C}_{RI}\dot{\mathbf{D}}_I-\mathbf{m}_{RI}\ddot{\mathbf{D}}_W\end{bmatrix} \tag{17}$$

2.3. Establishment of the dynamic equation of motion

After assembling the dynamic matrices of each sub-system and their interaction systems, the dynamic equation of motion of the vehicle-track-transition zone interaction system can be established in a fully coupled form, written as

$$\begin{bmatrix}\mathbf{K}_{VV}&\mathbf{K}_{VI}\\\mathbf{K}_{IV}&\mathbf{K}_{II}\end{bmatrix}\begin{bmatrix}\mathbf{x}_V\\\mathbf{x}_I\end{bmatrix}+\begin{bmatrix}\mathbf{C}_{VV}&\mathbf{C}_{VI}\\\mathbf{C}_{IV}&\mathbf{C}_{II}\end{bmatrix}\begin{bmatrix}\dot{\mathbf{x}}_V\\\dot{\mathbf{x}}_I\end{bmatrix}+\begin{bmatrix}\mathbf{M}_{VV}&0\\0&\mathbf{M}_{II}\end{bmatrix}\begin{bmatrix}\ddot{\mathbf{x}}_V\\\ddot{\mathbf{x}}_I\end{bmatrix}=\begin{bmatrix}\mathbf{F}_V\\\mathbf{F}_I\end{bmatrix} \tag{18}$$

with

$$\mathbf{M}_I=\begin{bmatrix}\mathbf{M}_{TT,t}&0&0\\0&\mathbf{M}_{B,t}&0\\0&0&\mathbf{M}_{S,t}\end{bmatrix},\ \mathbf{C}_I=\begin{bmatrix}\mathbf{C}_{TT,t}&\mathbf{C}_{TB,t}&\mathbf{C}_{TS,t}\\\mathbf{C}_{BT,t}&\mathbf{C}_{B,t}&0\\\mathbf{C}_{ST,t}&0&\mathbf{C}_{S,t}\end{bmatrix},\ \mathbf{K}_I=\begin{bmatrix}\mathbf{K}_{\mathrm{TT,t}}&\mathbf{K}_{\mathrm{TB,t}}&\mathbf{K}_{\mathrm{TS,t}}\\\mathbf{K}_{\mathrm{BT,t}}&\mathbf{K}_{\mathrm{B,t}}&0\\\mathbf{K}_{\mathrm{ST,t}}&0&\mathbf{K}_{\mathrm{S,t}}\end{bmatrix},$$

where *T, B,* and *S* represent track system, bridge, and subgrade, respectively; $\mathbf{x}$, $\dot{\mathbf{x}}$ and $\ddot{\mathbf{x}}$ represent the displacement, velocity, and acceleration vectors.

2.4. Validation of the dynamic model

To validate the accuracy of the dynamic model coded by MATLAB. a comparison to the model by Zhai is conducted. It is assumed that a vehicle runs on the transition zone (100~200m) at 350 km/h and rail adds initial irregularity (Refer to Fig. 10).

Fig. 5 shows the dynamic response of wheel load force in the transition zone compared with the Zhai et al. [27] model. The analysis shows that the dynamic results are consistent in both the first and fourth rounds of matching, thus further establishing the validity of the model. Because Zhai et al. [27] use modal superposition, which is different from the method adopted in this paper, there will be slight errors.

3. Mapping relationship model

In this section, a mapping relationship model for describing the deformation behavior of track and bridge under the pier settlement is proposed. Comparison between the proposed mapping relationship model and the theoretical model in Ref. [21] is conducted to illustrate the accuracy and effectiveness of the proposed model.

3.1. Mapping the relationship model

Supposing the pier settlement of the transition zone is $\boldsymbol{\delta}$, and then the "setting 0 to 1" method is adopted. The track deformation can be calculated as follows:

$$\begin{bmatrix} \overline{\Omega} & \mathbf{0} & \dots & \mathbf{0} \\ \mathbf{0} & & & \\ \vdots & & \mathbf{K}_S & \\ \mathbf{0} & & & \end{bmatrix} \begin{Bmatrix} \boldsymbol{\delta} \\ \vdots \\ \mathbf{X}_S \\ \vdots \end{Bmatrix} = \begin{Bmatrix} \overline{\mathbf{F}} \\ \vdots \\ \widetilde{\mathbf{F}} \\ \vdots \end{Bmatrix} \tag{19}$$

with $[\overline{\Omega}] = \begin{bmatrix} 1 & 0 & \dots & 0 \\ 0 & 1 & \dots & 0 \\ \vdots & \vdots & \ddots & \vdots \\ 0 & 0 & \dots & 1 \end{bmatrix}$ where $\overline{\mathbf{F}} = \boldsymbol{\delta}$ is the pier settlement of the corresponding degree of freedom. $\mathbf{K}_S$ denotes the stiffness matrix of system is not affected by pier settlement. Due to the nonlinear interaction between the bridge and baseplate or the baseplate and subgrade, the contact-separation problems are addressed by the compensation and removal of springs, as opposed to penalty function as traditional method. The internal forces should be expressed as piecewise functions, and the total internal forces of the system need to be determined by piecewise functions and *Newton-Raphson iterative method*, as shown in Fig. 6. The application of the method and its solution in the FE model is summarized as follows:

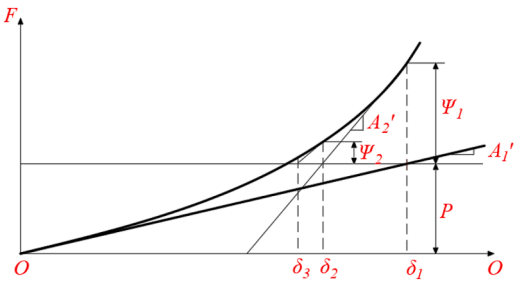

Fig. 6. Diagram of the Newton-Raphson iterative process.

(1) Consider the piecewise functions of the stiffness matrix as follows:

$$[\boldsymbol{\Lambda}(\delta)] = [\boldsymbol{\Psi}(\delta)] + [\widetilde{\Psi}(\delta)]\mathbf{l}(\{\boldsymbol{\delta}\} - \{\boldsymbol{\Lambda}\}) \tag{20}$$

where Ψ and $\widetilde{\Psi}$ denote the system's own stiffness matrix and the stiffness matrix governing interactions between its components, respectively; ℓ is a function that yields a positive value, denoted as:

$$\ell(x) = \begin{cases} 0; x < 0 \\ 1; x \geq 0 \end{cases} \tag{21}$$

(2) Compared with the traditional *Newton-Raphson iterative method*, the total internal force of the system can also be expressed in the form of a piecewise function, denoted as:

$$\{\boldsymbol{\Gamma}\} = [\boldsymbol{\Psi}(\delta)]\{\boldsymbol{\delta}\} + [\widetilde{\Psi}(\delta)](\{\boldsymbol{\delta}\} - \{\boldsymbol{\Lambda}\})\ell(\{\boldsymbol{\delta}\} - \{\boldsymbol{\Lambda}\}) - \{\mathbf{P}\} \tag{22}$$

(3) Combined the *Newton-Raphson iterative method* and the equation of the total internal forces of the system, the final solution of the formulation can be expressed as:

$$\begin{cases} \{\boldsymbol{\delta}^{n+1}\} = \{\boldsymbol{\delta}^n\} - [\mathbf{T}]^{-1}([\boldsymbol{\Psi}(\boldsymbol{\delta}^n)]\{\boldsymbol{\delta}^n\} + [\widetilde{\Psi}(\boldsymbol{\delta}^n)](\{\boldsymbol{\delta}^n\} - \{\boldsymbol{\Lambda}\})\ell(\{\boldsymbol{\delta}^n\} - \{\boldsymbol{\Lambda}\}) - \{\mathbf{P}\}) \\ [\mathbf{T}] = [\boldsymbol{\Psi}'(\boldsymbol{\delta}^n)] + [\widetilde{\Psi}'(\boldsymbol{\delta}^n)]\ell(\{\boldsymbol{\delta}^n\} - \{\boldsymbol{\Lambda}\}) \end{cases} \tag{23}$$

where $\mathbf{T}$ represents the tangent stiffness of matrix.

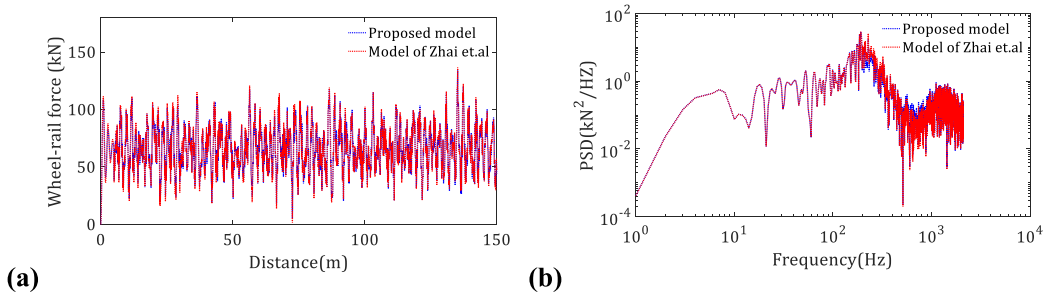

Fig. 5. Comparisons with the model of Zhai (a. wheel-rail force; b. PSD curve;).

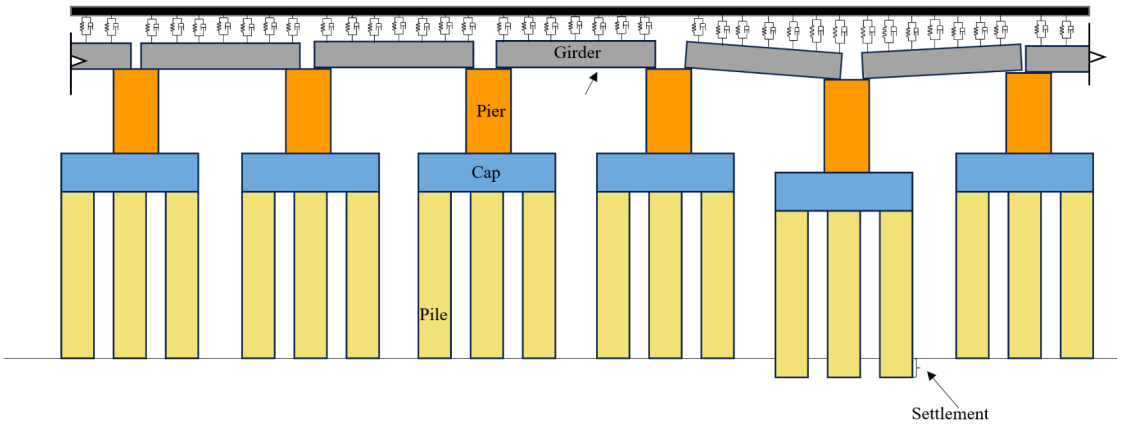

Fig. 7. Settlement diagram of bridge pier.

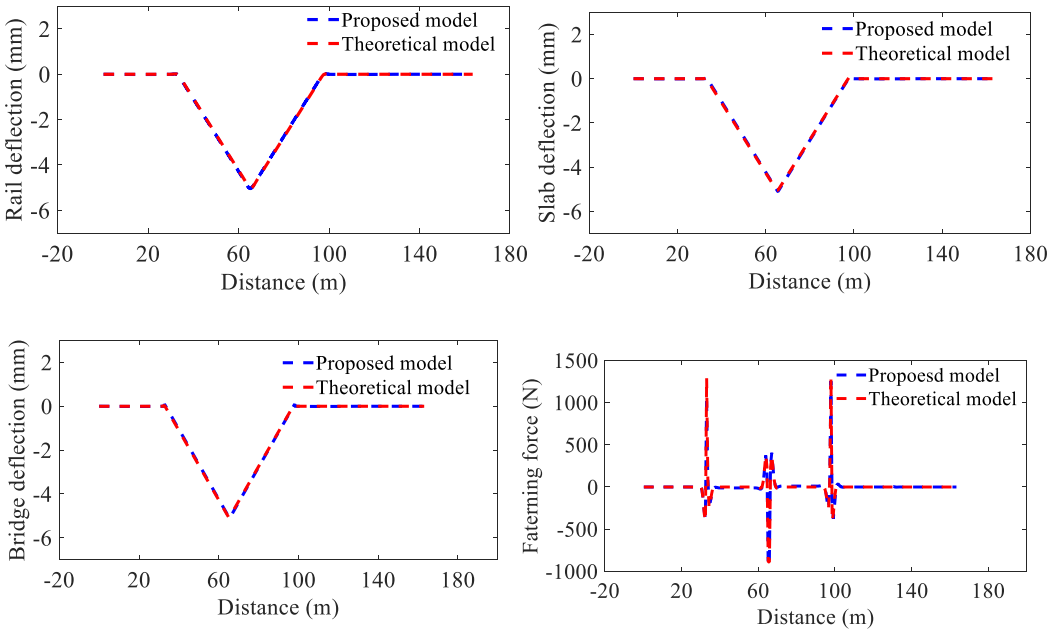

Fig. 8. Result comparison (a. rail deformation, b. slab deformation, c. bridge deformation, d. fastener force).

3.2. *Validation of the mapping relationship model*

In previous studies [21-24], the mapping relationship between pier settlement and rail deformation is simulated by the theoretical solution models (Ref. [21]), which have been widely used in this field. In this paper, in order to verify the accuracy of the finite element model, a 5-span simply-supported beam bridge was established, as shown in Fig. 7, with pier No. 1-6 as the index, and the parameters of the model are shown in **Appendix III**. The settlement of 5mm is set in Pier 3, and the comparison is made between the proposed model and the theoretical model. Fig. 8**(a)** shows the rail deformation under the proposed model and the theoretical model, and the maximum difference between them is less than 3%. The slab and bridge girder deformation under the above two models are shown in Fig. 8**(b)** and Fig. 8**(c)** respectively, and the maximum difference is also less than 3%. Compared with the theoretical model, the effect of the slab forces on the deformation of the bridge structure is considered under the proposed model.

The fastener force derived from the pier settlement is shown in Fig. 8 **(d)**, and it is easy to find that the fastener force significantly affects pier2, pier3, and pier4 and peaks at the gap of the bridge pier. It can be found that the maximum difference in the fastener force between the theoretical model and the proposed model is still less than 3%.

By comparing and analyzing the above results, the proposed model is found to be accurate and applicable, the maximum values of the comparison results are shown in Table 1.

Table 1
Comparison result.

Calculation Result	Maximum value of rail deformation/mm		Fastener force peak/N	
	Upward deformation	Downward deformation	Tensile force	Compressive force
Proposed model	0.027	5.036	927.182	1074.99
Theoretical model	0.011	5.022	888.566	1292.460

4. Numerical studies

In this section, two illustrative cases are performed to discuss the dynamic effects of the pier settlement and subgrade bending settlement on the vehicle-track-transition zone interaction system. The different vehicle running speeds and transition zone lengths are set in the

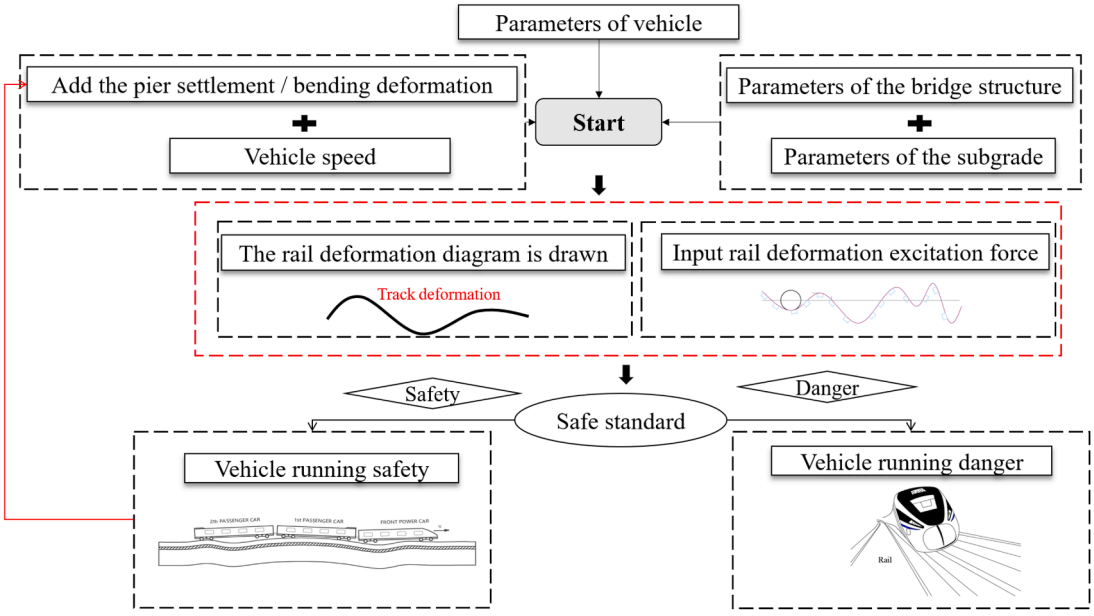

Fig. 9. Flow chart of the analysis framework for the vehicle running safely in settlement.

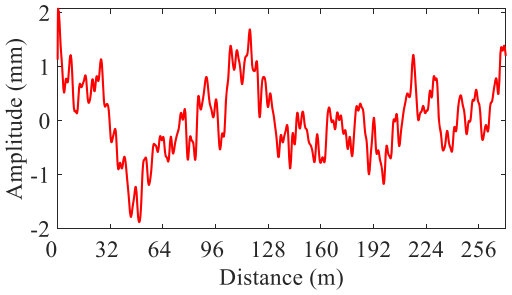

Fig. 10. Initial vertical track irregularity.

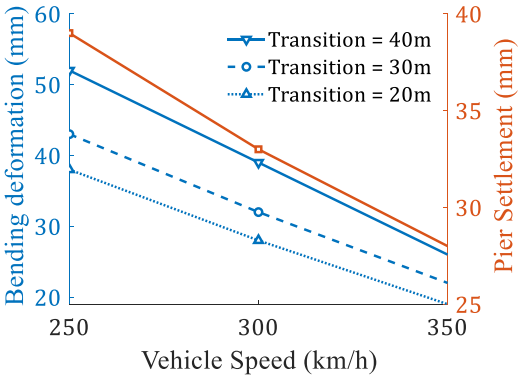

Fig. 11. Foundation settlement threshold.

parametric studies to evaluate the riding safety of high-speed train, in this case, the settlement thresholds can be determined and calibrated.

4.1. The simulation parameters and calculational conditions

The simulation parameters of the train, track can be found in Ref. [31], while the bridge and subgrade has been listed in **Appendix**. In the simulation model, the length of the transition zone is 270 m. The running mileage of the high-speed train is 256 m. Considering the wheel-load force and vehicle acceleration is more sensitive for the foundation settlement. The rate of wheel load reduction is suitable for the safety standard. The flow chart of the analysis procedure is shown in Fig. 9.

The initial rail irregularity, as depicted in Fig. 10, is considered as the additional vertical rail irregularity which combines with rail deformation caused by foundation settlement to study riding safety by time-frequency method. This enables an exploration of parameter trends under different working conditions.

By employing the analysis framework, Fig. 11 shows the settlement threshold including pier settlement and bending deformation of foundation settlement under different vehicle speed. It can be observed that the settlement threshold decreases with the vehicle speed rising. It is noteworthy that the, the settlement threshold is directly proportional to the length of the transition zone at the same velocity. The results show the vehicle speed and length of transition zone play an important role in foundation settlement.

4.2. Impact of pier settlement on riding safety

Fig. 12 illustrates the rules of wheel-rail forces and body accelerations in the main rail deformation area under the different settlement amplitudes of pier 6. It can be observed that with the increase of pier settlement, the rail bending angle increases obviously. The minimum relative displacement between the wheel and rail in the rail bending angle area decreases continuously, resulting in the decrease of wheel load mutation value and the increase of wheel load reduction rate, which has an impact on riding safety. Moreover, the maximum acceleration of the car body also increases, resulting in reduced riding comfort. With the increase in the vehicle speed, the interaction between the wheel and rail generally decreases. Therefore, when the vehicle approaches the rail bending angle region, the peak of wheel load mutation is relatively small, leading to non-compliance with the specified wheel weight reduction rate.

When the CRH380A vehicle passes the transition zone at 350km/h, the settlement threshold of Pier 6 is 28mm. Assuming that the initial irregularity of the track is not considered when the vehicle is traveling at the speed of 350 km/h in the transition zone, the track will undergo different dynamic deformation as the vehicle moves forward. The dynamic deformation of the rail can be directly reflected in the program with a spatial-temporal relationship, as shown in Fig. 13. In the settlement area, the vehicle-rail interaction is weakened in the process

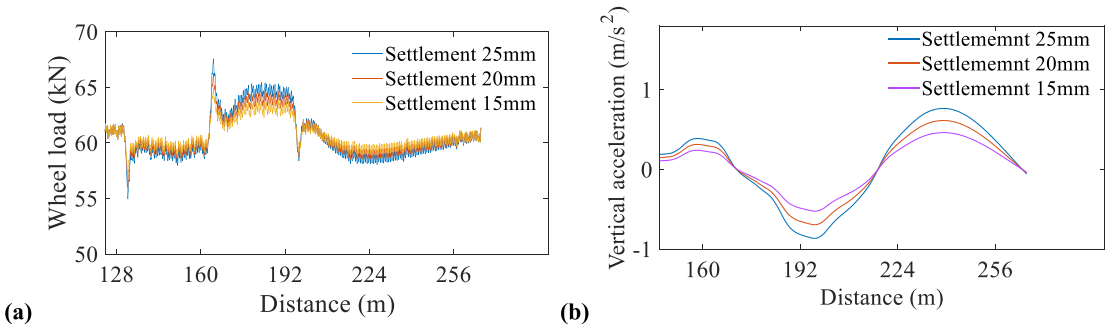

Fig. 12. Influence of pier settlement on dynamic response (a. wheel load force; b. car body acceleration).

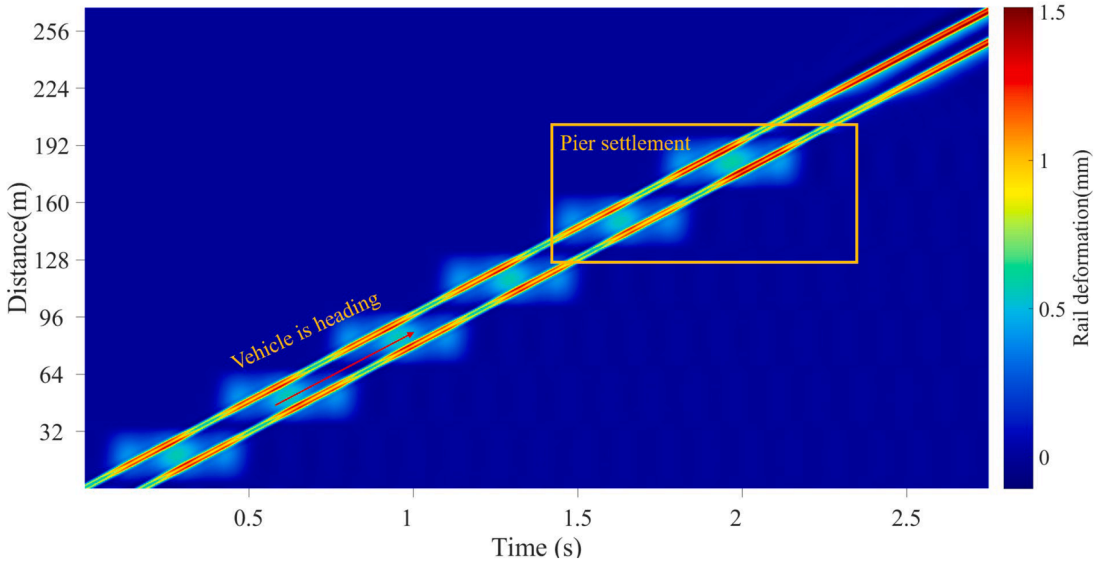

Fig. 13. Rail deformation in the space-time domain.

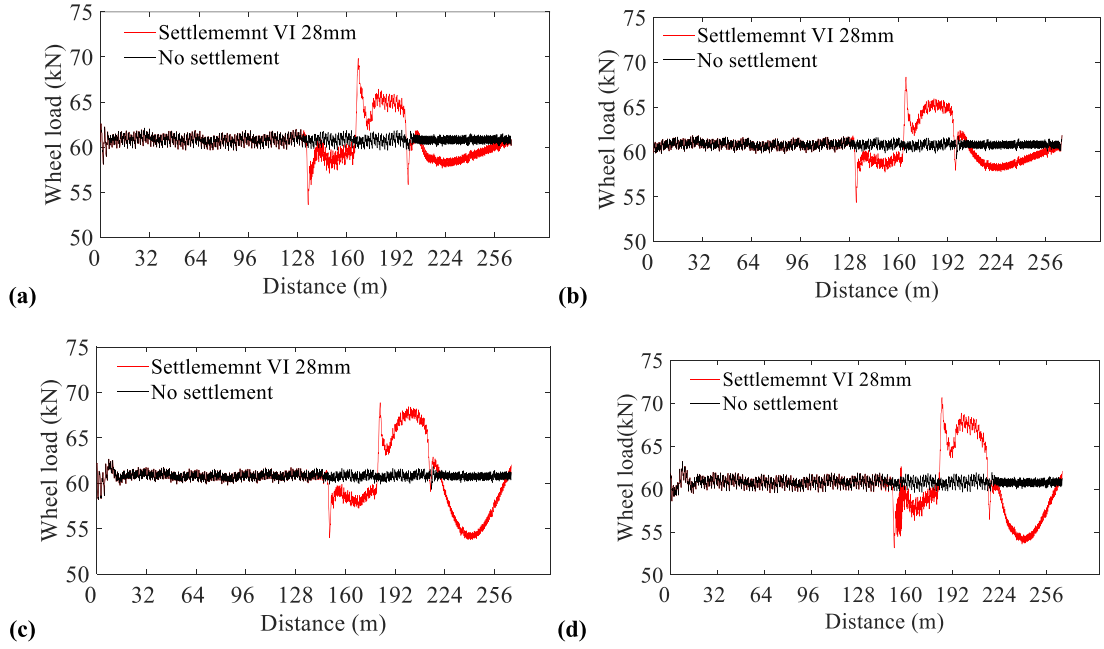

Fig. 14. Wheel-rail force of four wheelsets (a. wheel 1; b. wheel 2; c. wheel 3; d. wheel 4).

downhill, while the train-rail interaction is enhanced in the process of uphill. The maximum dynamic displacement of the rail is 1.2mm and 1.35mm respectively, during the process of uphill and downhill in the settlement region. Compared with the maximum displacement of the rail in the non-settling area, which is 1.3mm, the deformation is decreased by 7.7% and increased by 3.5%, respectively.

In order to better investigate and judge the riding safety in the transition zone under pier settlement, the wheel-rail forces of the different wheels are calculated, as shown in Fig. 14. Through analysis, it can be concluded that when the vehicle approaches the settled girder, the relative displacement between the wheel and rail undergoes a sudden decrease caused by the rail bending angle deformation, resulting in the sudden decrease in the wheel-rail forces. When the vehicle approaches the gap between settling girders, an increase in the relative displacement between the wheel and the rail leads to a surge in the wheel-rail force to the maximum value. When the vehicle travels between the settling girders, the variation rate in the relative displacement becomes gradual, causing the wheel-rail force to approach a stable value. Through the analysis of the wheel-rail force in the transition zone, it can be found that due to the gradual variation in soil stiffness from high to low in the transition zone, the relative displacement between the wheel and rail initially decreases and then increases, and finally approaches a fixed value. Through the analysis of wheel force in the four wheelsets, it can be found that under the pier settlement, the wheel-rail force in the fourth wheelset exhibits the highest sensitivity and is more prone to jump rail.

The vehicle body acceleration, as displayed in Fig. 15, shows a certain degree of lag and similarity compared to the wheel-rail force. This is because the vehicle body is connected to two bogies, resulting in the generation of two similar waveforms when the vehicle passes through the rail bending angle deformation area.

To further explore the rule between pier settlement and traffic safety, additional vertical rail irregularity simulation is added to the time-frequency analysis. In this paper, Stockwell et al. [36] method is used for time-frequency analysis, which is defined:

$$S(\tau,f)=\int_{-\infty}^{\infty}h(t)\frac{|f|}{\sqrt{2\pi}}e^{-\frac{(\tau-t)^2f^2}{2}}e^{-i2ft}dt \tag{24}$$

where τ which controls the position of the window function along the time axis represents time; $h(t)$ represents the analysis signal; $S(\tau, f)$ is the transformed time-frequency spectrum matrix. For discrete signals, $f=n/NT$, $\tau=jT$ the final signal can be represented as:

$$S\left(jT,\frac{n}{NT}\right)=\sum_{m=0}^{N-1}H\left[\frac{m+n}{NT}\right]e^{-\frac{2\pi^2m^2}{n^2}}e^{-\frac{i2\pi mj}{N}}(n\neq 0) \tag{25}$$

The advantage of this method is that it overcomes the limitation of fixed time width in STFT window by adaptively adjusting the analysis time width based on frequency changes, thereby providing intuitive time-frequency features without the need for selecting window functions or dividing scales.

The pier experiences a 20mm settlement and the vehicle is traveling

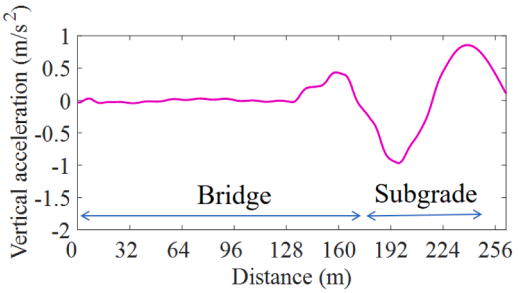

Fig. 15. The acceleration of the car body.

at 350 km/h, the impact of pier settlement on the time-frequency characteristic of wheel force is explored, and the time-frequency characteristic of wheel force is analyzed, as shown in Fig. 16. It can be obtained from Fig. 16 **(a)** that the wheel force, when the initial vertical irregularity, is only introduced, is mainly distributed at the low-frequency range (45~50Hz), indicating a heightened sensitivity to excitations within this range. Compared with Fig. 16 **(a)**, The wheel-rail force experiences excitation at the high-frequency range (250-500Hz) under combined the pier settlement and initial vertical irregularity, which can be attributed to the abrupt upwarp of the rail, as shown in Fig. 16 **(b)**. Moreover, the wheel-rail force is notably amplified at the frequency range of 200~500Hz. The rail bending angle deformation will lead to a sudden change in the wheel-rail force, and from 1.3s to 1.4s, the wheel-rail force is mainly stimulated within the high-frequency range.

Fig. 17 illustrates the relationship between wheel-rail force and pier settlement, assuming that the initial irregularity is not incorporated into the time-frequency analysis. When the vehicle approaches the rail bending angle area, the wheel-rail force is strengthened at the frequency of 20-60 Hz and stimulated at the high frequency of 400-500Hz. It means that the wheel load force changes abruptly and the pier settlement can greatly affect the riding safety performance. Compared with the wheel load forces where the initial irregularity is incorporated, as shown in Fig. 16**(a)**, it is evident that under the influence of initial irregularity, there is an increased risk of abrupt changes in wheel-rail force, resulting in a lower settlement threshold.

4.3. Impact of bending deformation on riding safety

As discussed in Ref. [9,10,11], the bending deformation often occurs at the transition zone due to the variation stiffness of the subgrade. The deterioration degree of transition is defined by bending angle, and the scheme of that is shown in Fig. 18.

Employing a quantitative analytical approach, vehicles are tested at speeds of 350 km/h, 300 km/h, and 250 km/h, traversing a 20-meter transition section with a bending deformation of 18 mm. The schematic representation of wheel load forces in the primary rail deformation is depicted in Fig. 19**(a)**. As the speed increases, the abrupt change in the wheel-load force caused by the upward deformation of the rail at the intersection of the bridge pier and subgrade increases, thus affecting riding safety. In terms of the convergence speed of wheel load force, it can be found that the vehicle speed has no impact on the convergence speed of wheel load force.

When the vehicle traverses the transition zone with an 18 mm bending deformation, the length of the transition zone is set as 20m, 30m, and 40m respectively, and the corresponding wheel load forces are shown in Fig. 19**(b)**. It can be found that as the length of the transition zone increases, the abrupt change in the wheel load forces at the same location gradually reduces, thereby impacting the safety performance of the vehicle. To enhance vehicle safety appropriately, it is advisable to extend the length of the transition zone. When the CRH380A train moves at 350 km/h through a bridge-subgrade transition zone with a length of 20 m and a bending deformation of 19 mm ($\theta_R = 0.95\%$), the dynamic response is analyzed based on the previously mentioned approach. the dynamic response of the bending deformation of the transition zone is further analyzed, which is similar to the research on traffic safety in the transition zone under pier settlement. Fig. 20 is a spatiotemporal nebula diagram illustrating the rail dynamic deformation. Through comparative analysis, it can be seen that the bending deformation reduces the rail deformation under wheels in the bridge-subgrade transition zone to a certain extent. As the train approaches the middle of the transition zone, the rail deformation measures 0.72mm under the presence of bending deformation, as compared to 0.76mm when there is no bending deformation, marking 6% reduction. During the period from the first wheelset's passage through the deformed section to the fourth wheelset's passage through the deformed section, there is a noticeable increase in rail deformation under the first and

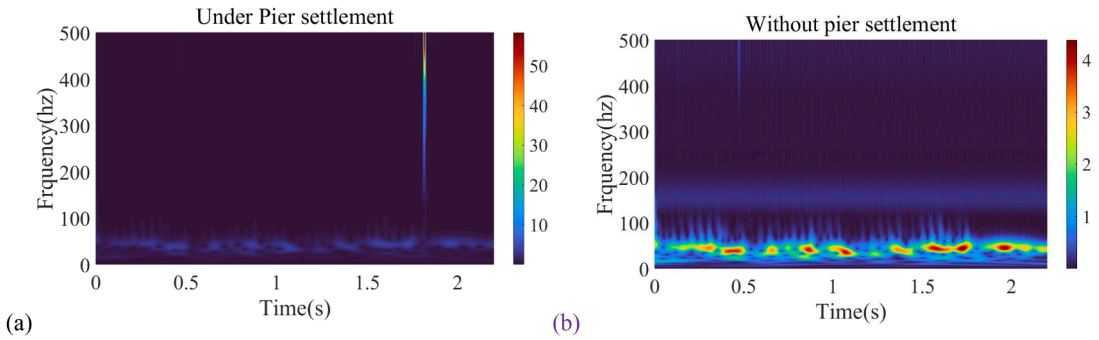

Fig. 16. Wheel-rail force (a. under pier settlement; b. without pier settlement) in time-frequency domain.

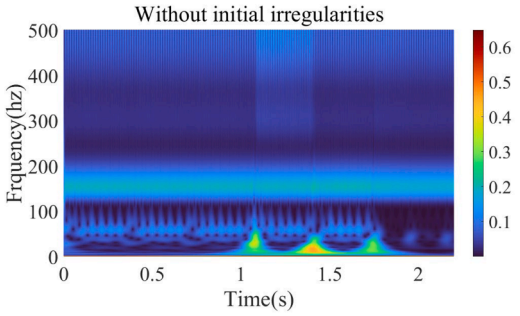

Fig. 17. Wheel load force without irregularity in the time-frequency domain.

second wheelsets.

Fig. 21 shows the changes in wheel load force and car body acceleration under the working conditions mentioned above. The bending deformation of the subgrade will cause an upward tilting of the rail at the beginning and end of the transition zone. When the wheel approaches the starting point of the bridge-subgrade transition zone, a sudden change in wheel load force occurs due to the upward tilting of the rail and the abrupt variations in the stiffness of the bridge and subgrade. On the contrary, when the stiffness of the transition zone changes slowly, the relative displacement between the wheel and the rail increases, resulting in a sudden decrease in the wheel load force. When the vehicle reaches the end of the bridge-subgrade transition zone, although the upward tilting of the rail is more obvious than that at the starting point, the gradual transition in stiffness results in a less obvious abrupt change in the wheel load force, thereby effectively elevating the threshold of traffic safety. The maximum acceleration value of the car body is less than 0.13 g, satisfying the basic riding comfort requirement. when a vehicle travels at 350 km/h through the transition zone with a 15mm bending deformation and the additional vertical rail irregularity is incorporated, the time-frequency analysis of the wheel-rail force is shown in Fig. 22**(a)**. It can be observed that when the vehicle reaches the point of rail tilting within the time range of 1.9-2s, there is a significant variation in the frequency and the wheel load force is primarily stimulated by the high-frequency part. Moreover, the bending deformation of the transition zone will cause a sudden change in the wheel load force and finally affect riding safety.

Under the same working conditions as above, we further analyze the wheel load force when the vehicle travels at 250km/h through the deformation area of the transition zone. As can be seen from Fig. 22**(b)**,

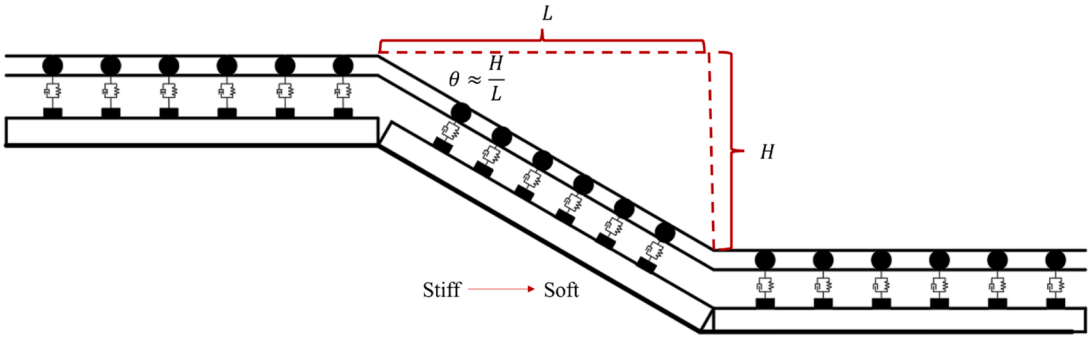

Fig. 18. Schematic of bending deformation.

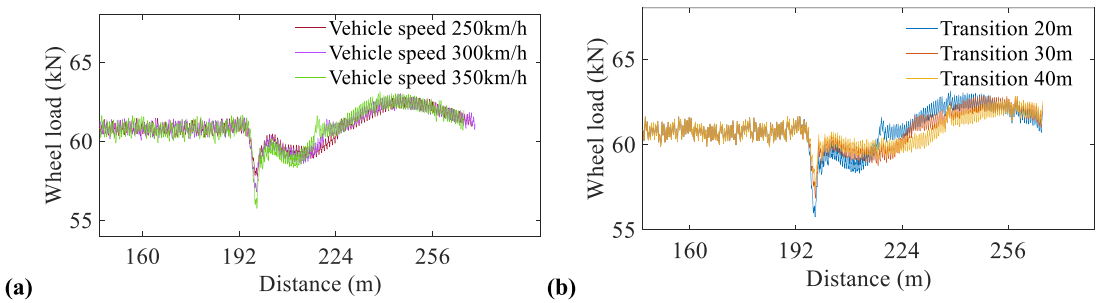

Fig. 19. Influence of bending deformation on dynamic response (a. vehicle speed; b. transition length).

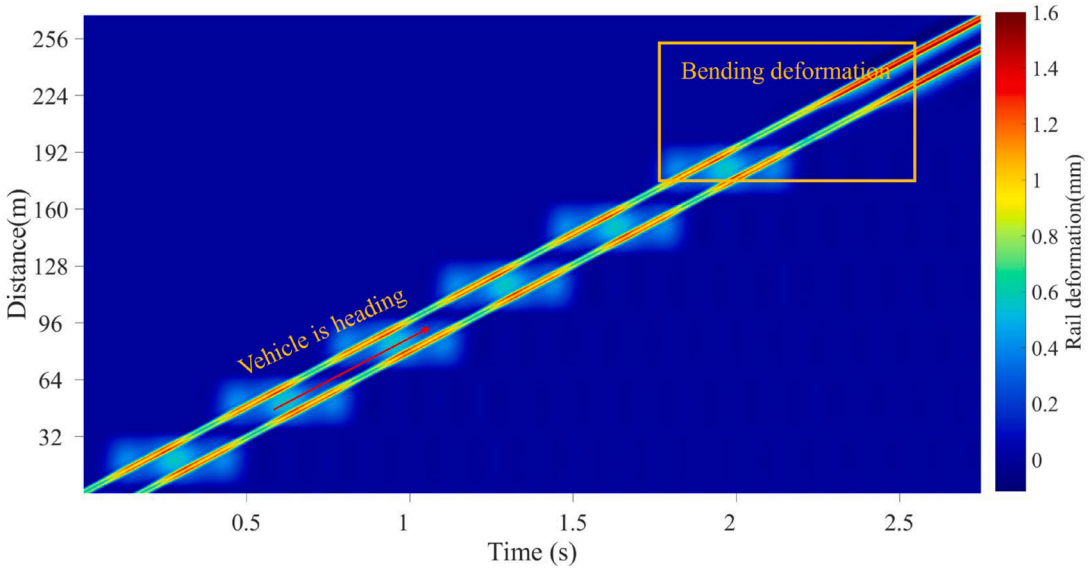

Fig. 20. Rail deformation in the space-time domain.

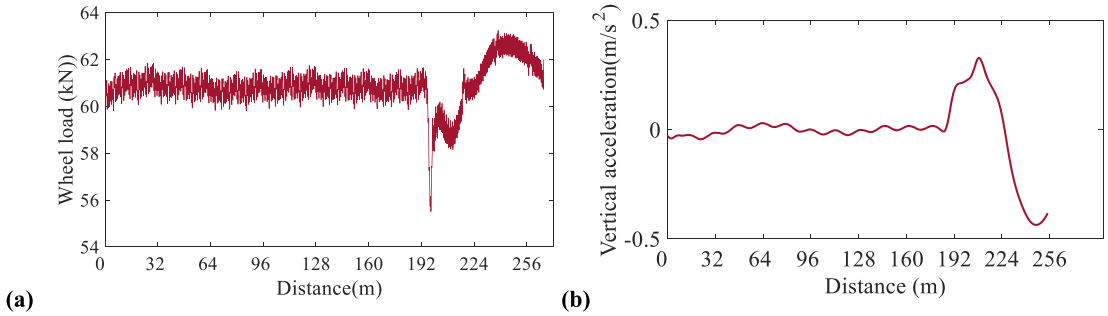

Fig. 21. Dynamic response caused by bending deformation (a. wheel load force; b. car body acceleration).

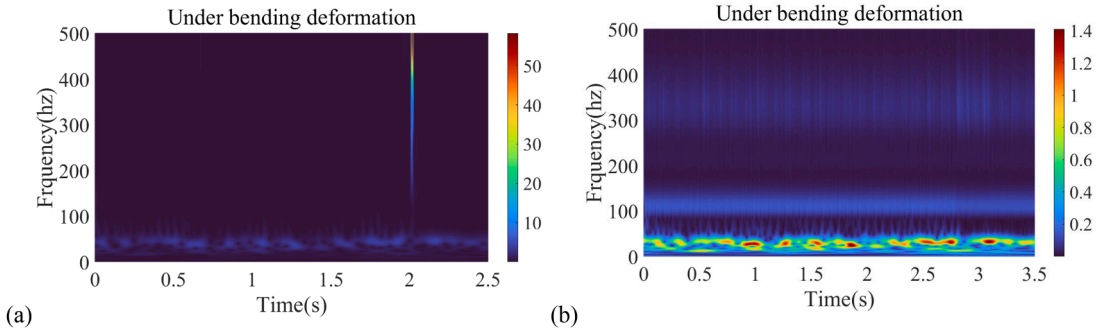

Fig. 22. Wheel load force under bending deformation in the time-frequency domain (a. 350 km/h; b. 250 km/h).

from 2.5s to 3s, the wheel-rail force of the vehicle is still mainly stimulated in the range of 20 - 60Hz, which reflects that the speed reduction can effectively prevent the sudden change of wheel load force. Therefore, it can be concluded that reducing the speed can effectively improve the riding safety performance under the bending deformation of the transition zone.

5. Concluding remarks

In this work, an effective numerical model is established to investigate the bending deformation caused by the settlement behavior of the transition zone, and dynamic analysis is performed to reveal the response rule subjected to the settlement. The two proposed models, namely the dynamic interaction model and the mapping relationship model are validated by comparing the results with that of others' work. There are several concluding remarks can be drawn from the numerical study, as follows:

(1) From the dynamic response, the amplitude of foundation settlement affects the wheel-rail force and the car body of vertical acceleration in the pier settlement region. With the increase of the amplitude of foundation settlement from 15~25, the wheel load force increases range from 5% to 10%. The length of the transition zone has a great influence on the dynamic response of

train. With the length of transition from 20 to 35, the abrupt change in the wheel load forces has been reduced from 58.2 kN to 56.1 kN.

(2) The reduction of the train speed is beneficial to the riding safety. With the train speed increases, the value of most adverse like load reduction rate is greater, resulting in the reduction of the settlement threshold. When the train speed is 250 km/h, 300 km/h, 350 km/h., the threshold of the foundation settlement reduction rate is 10∼30%.

(3) The influence of rail irregularity on the dynamic performance is analyzed by using the time-frequency method. The additional vertical rail irregularity will deteriorate the wheel-rail force, and the amplitude is easily excited by the high-frequency load induced by the rail bending deformation. Compared to the foundation settlement, the dynamic effect of the initial rail irregularity on the wheel-rail system is mainly at the frequency of 45∼50 Hz, while the responses at 250-∼500 Hz are mainly excited by the foundation settlement, which illustrates that the bending deformation severely aggravates the dynamic safety of the train and substructures.

CRediT authorship contribution statement

Borong Peng: Writing – original draft, Methodology, Formal analysis, Conceptualization. **Xuhui He:** Funding acquisition. **Lei Xu:** Validation, Investigation. **Zheng Li:** Writing – review & editing, Methodology. **Yunlong Guo:** Methodology, Conceptualization.

Declaration of competing interest

The authors declare that they have no known competing financial interests or personal relationships that could have appeared to influence the work reported in this paper.

Data availability

Data will be made available on request.

Acknowledgment

This work was supported by the National Natural Science Foundation of China (Grant No. U1934209). The European Commission and UKRI Engineering and Physical Science Research Council (EPSRC) are acknowledged for the financial sponsorship of Re4Rail project (Grant No EP/Y015401/1).

Appendix

I. The parameters of the CRST I baseplate

Infrastructure	Width(m)	height(m)	Number of the slab
Bridge	3	0.302	1
Subgrade	2.8	0.281	4

II appendix of the parameters of the transitionx

Description	Young modulus E (MPa)	Poisson's rationv(-)	Density ρ(g/cm^3)	Height(m)
Gravel layer	400	0.25	1.3	0.4
Graver fill	300	0.25	1.2	5
Protection layer	180	0.25	2	0.4
Subgrade surface	110	0.25	1.8	2.7
Subgrade	60	0.25	1.7	2.3

III the parameters of the model

Components	Elastic modulus (GPa)	Poisson's ratio	Moment of inertia (mm^4)	Vertical spring stiffness(N/m)
Rail	210	0.3	3217×10^7	——
Slab	36.5	0.2	1372×10^9	——
Base slab	34	0.2	1867×10^9	——
Girder	35.5	0.2	1086×10^{13}	——
Fastener	——	——	——	3.7×10^8
CA mortar layer	0.2	0.2	——	4.5×10^8
Strong spring	——	——	——	1.0×10^{11}
Bearing	——	——	——	3.0×10^9

Reference

[1] Connolly D, Marecki G, Kouroussis G. The growth of railway ground vibration problems - A review. Science of the Total Environment 2016;568(oct.15):1276–82.

[2] Zhai W, Wang K, Chen Z, et al. Full-scale multi-functional test platform for investigating mechanical performance of track–subgrade systems of high-speed railways. Railway Engineering Science 2020;28(3):213–31.

[3] Zhai W, Han Z, Chen Z, Ling L, Zhu S. Train–track–bridge dynamic interaction: a state-of-the-art review. Vehicle System Dynamics 2019;57(7):984–1027.

[4] Li D, Davis D. Transition of railroad bridge approaches. J. Geotech. Geoenviron. Eng. 2005;131(11):1392–8.
[5] Coelho B, et al. An assessment of transition zone performance. Proc. Inst. Mech. Eng. - Part F J. Rail Rapid Transit. 2011;225(2):129–39.
[6] Stark TD, Wilk ST. Root cause of differential movement at bridge transition zones. Proc. Inst. Mech. Eng. - Part F J. Rail Rapid Transit. 2015;230(4):1257–69.
[7] Kerr AD, Moroney BE. Track transition problems and remedies. Proc. Am. Railway Eng.Assoc. 1993 94-25.
[8] Paixao A, Fortunato E, Calcada R. Design and construction of backfills for railway track transition zones. Proc. Inst. Mech. Eng. - Part F J. Rail Rapid Transit. 2013; 229(1):58–70.
[9] Wang HY, Markine VL. Methodology for the comprehensive analysis of railway transition zones. Computers and Geotechnics 2018;99:64–79.
[10] Wang HY, Markine V. Dynamic behaviour of the track in transitions zones considering the differential settlement. Journal of Sound and Vibration 2019;459.
[11] Wang HY, Markine V. Modelling of the long-term behaviour of transition zones: Prediction of track settlement. Engineering Structures 2018;156:294–304.
[12] Shan Y, Zhou SH, Zhou HC, Wang BL, Zhao ZC, Shu Y, Yu Z. Iterative Method for Predicting Uneven Settlement Caused by High-Speed Train Loads in Transition-Zone Subgrade. Transportation Research Record 2017:7–14.
[13] Shan Y, Zhou SH, Wang BL, Ho CL. Differential Settlement Prediction of Ballasted Tracks in Bridge-Embankment Transition Zones. Journal of Geotechnical and Geoenvironmental Engineering 2020;146.
[14] Varandas JN, Hölscher P, Silva MAG. Settlement of ballasted track under traffic loading: Application to transition zones. Proceedings of the Institution of Mechanical Engineers Part F-Journal of Rail and Rapid Transit 2014;228:242–59.
[15] Varandas JN, Hölscher P, Silva MAG. Dynamic behaviour of railway tracks on transitions zones. Computers & Structures 2011;89:1468–79.
[16] Paixao A, Fortunato E, Calçada R. A numerical study on the influence of backfill settlements in the train/track interaction at transition zones to railway bridges. Proceedings of the Institution of Mechanical Engineers Part F-Journal of Rail and Rapid Transit 2016;230:866–78.
[17] Nasrollahi K, Nielsen JCO, Aggestam E, Dijkstra J, Ekh M. Prediction of long-term differential track settlement in a transition zone using an iterative approach. Engineering Structures 2023;283.
[18] Sun Y, Zhai WM. Long-term prediction of track geometry degradation in high-speed vehicle–ballastless track system due to differential subgrade settlement. Soil dynamic and earthquake engineering 2018;113:1–11.
[19] Chen ZW, Sun Y, Zhai WM. Mapping relationship between pier settlement and rail deformation of high-speed railways-part (I): The unit slab track system. Sci. China: Tech. Sci. 2014;44(7):770–7.
[20] Chen ZW, Zhai WM, Cai CB, Sun Y. Safety threshold of high-speed railway pier settlement based on train-track-bridge dynamic interaction. Science China-Technological Sciences 2015;58:202–10.
[21] Chen ZW, Zhai WM. Theoretical method of determining pier settlement limit value for China's high-speed railway bridges considering complete factors. Engineering Structures 2020:209.
[22] Chen ZW, Fang H. Influence of pier settlement on contact behavior between CRTS II track and bridge in high-speed railways. Engineering Structures 2021;235.
[23] Gou HY, Ran ZW, Yang LC, Bao Y, Pu QH. Mapping vertical bridge deformations to track geometry for high-speed railway. Steel and Composite Structures 2019;32: 467–78.
[24] Gou HY, He YN, Zhou W, Bao Y, Chen GD. Experimental and numerical investigations of the dynamic responses of an asymmetrical arch railway bridge. P. I. Mech. Eng. F-J. RAI. 2018;232(9):2309–23.
[25] Yau JD. Response of a train moving on multi-span railway bridges undergoing ground settlement. Engineering structures 2009;31:2115–22.
[26] Stone Jr Richard C, Farhangi Visar, Fatahi Behzad. A novel short pile foundation system bonded to highly cemented layers for settlement control. Canadian Geotechnical Journal 2024;60(9).
[27] Zhai WM, Wang S, Zhang N, Gao M, Xia H, Cai C, Zhao C. High-speed train-track-bridge dynamic interactions – Part II: Experimental validation and engineering application. International Journal of Rail Transportation 2013;1(1–2):25–41.
[28] Zhai WM, Wei K, Song X, Shao M. Experimental investigation into ground vibrations induced by very high-speed trains on a non-ballasted track. Soil Dynamics and Earthquake Engineering 2015;72:24–36.
[29] Xia H, Zhang N. Dynamic analysis of railway bridge under high-speed trains. Computers & Structures 2005;83(23–24):1891–901.
[30] Xia H, Guo W. Dynamic analysis of train-bridge system under differential settlement and scouring effect of foundations. Vol. 8 of Dynamic interaction of train-bridge systems in high-speed railways. Berlin: Springer; 2018.
[31] Xu L, Zhai W, Li Z. A coupled model for train-track-bridge stochastic analysis with consideration of spatial variation and temporal evolution. Applied Mathematical Modelling 2018;63:709–31.
[32] Li Z, Xu L, Wang DL, Niu ZJ, Zhao YS, Liu W, Zhan XS. 2D and 3D soil finite/infinite element models: modelling, comparison and application in vehicle-track dynamic interaction. International Journal of Rail Transportation 2023;11:339–63.
[33] Xie D. Soil dynamics. Beijing: Higher Education Press; 2011.
[34] Xu L, Li Z, Zhao YS, Yu ZW, Wang K. Modelling of vehicle-track related dynamics: a development of multi-finite-element coupling method and multi-time-step solution method. Vehicle System Dynamics 2022;60:1097–124.
[35] Xu L, Liu XM. Matrix coupled model for the vehicle-track interaction analysis featured to the railway crossing. Mechanical Systems and Signal Processing 2021; 152.
[36] Stockwell RG, Mansinha L, Lowe RP. Localization of the complex spectrum: the S transform. IEEE Transactions on Signal Processing 1996;44(4):998–1001.